

Structural performance of GFRP-concrete composite beams

Yong Yang, Yicong Xue*, Tao Zhang and Jing Tian

School of Civil Engineering, Xi'an University of Architecture and Technology, No. 13 Yanta Road, Xi'an, Shaanxi, China

(Received May 24, 2018, Revised October 10, 2018, Accepted October 11, 2018)

Abstract. This paper presents the results of an experimental study on the structural performance of an innovative GFRP-concrete composite beam construction, which is reinforced with longitudinal GFRP pultruded box-profile and transverse steel stirrups. GFRP perfobond (PBL) shear connectors are employed to enhance the bonding performance between the GFRP profile and the concrete portion. To investigate the shear and flexural performance of this composite system, eight specimens were designed and tested under three-point and four-point bending. The main variables were the height of the composite beam and the shear span-to-depth ratio. The test results indicated that bonding cracks did not occur at the interface between the GFRP profile and the concrete until the final stage of the test. This shows that the specimens performed well as composite beams during the test and that the GFRP PBL connectors were reliable. Based on the test results, two calculation methods were used to determine the flexural and shear capacity of the composite beams. A comparative study of the test and theoretical results suggests that the proposed methods can reasonably predict both the flexural and shear capacities of the specimens, whereas the provisions of ACI 440 are relatively conservative on both counts.

Keywords: GFRP-concrete composite beam; flexural performance; shear performance; experimental study; static load

1. Introduction

In recent decades, glass fibre-reinforced polymer (GFRP) composites have been widely applied in marine structures that are exposed to an aggressive atmosphere and should meet high standards of durable performance. Entire GFRP bridges were once regarded as an advisable solution to resist corrosion and enhance the durability of marine bridge systems; however, their relatively high costs hinder the development of entire GFRP bridge systems. Some researchers suggested the combination of GFRP and concrete to reduce the overall cost of a structure. Furthermore, concrete can efficiently enhance the compressive resistance and provide stability of the composite members.

Since then, some experimental research has been carried out on the structural behaviour of GFRP-concrete composite beams. Fam and Skutezky (2006) proposed composite T-beams using reduced-scale rectangular FRP tubes and concrete slabs. Hassanzadeh and Dehestani (2017) conducted numerical modelling of semi-confined composite beams consisting of GFRP and concrete. Aydın and Sarıbiyık (2013) proposed hybrid beams formed with GFRP box section and concrete. Unsal *et al.* (2017) explored the load-deflection behaviour of two-span continuous concrete beams reinforced with GFRP and steel bars. Muttashar *et al.* (2017) proposed multi-celled GFRP composite beams with concrete infill and explored their flexural behaviour. The mechanical performance of

composite beams reinforced with GFRP I-beams and steel bars was investigated by Hadi and Yuan (2017), and Huang *et al.* (2018) investigated the flexural performance of U-shape FRP profile-RC composite beams. Thomas and Ramadassa proposed a design method for shear strength of concrete beams longitudinally reinforced with GFRP bars.

The aforementioned research shows a high potential for GFRP-concrete composite beams in which each material is used optimally. However, it is a challenge to guarantee the composite action between two different materials and to find the optimal composite form. Neagoe *et al.* (2015) proposed GFRP-concrete hybrid beams with low degree of shear connection. Koaik *et al.* (2017) investigated the flexural performance of concrete-GFRP hybrid beams with bolt connectors. Zuo *et al.* (2018) and Xin *et al.* (2015) proposed GFRP composite deck systems with perforated rib connectors and conducted experiments to explore the fatigue and mechanical performance.

This study focuses on finding the optimal combination of GFRP-concrete composite beams, by including a concrete T-beam acting compositely with the GFRP box profile, using GFRP perfobond (PBL) shear connectors. Because the modulus of elasticity of GFRP profiles is lower than that of traditional steel reinforcements, it will lead to a lower flexural stiffness in GFRP-concrete composite beams, which may cause larger vertical deflection under normal work condition to compromise the serviceability. In this system, the reinforced concrete T-beam can effectively enhance the flexural stiffness of the entire member to avoid excessive vertical deflection. As illustrated in Fig. 1, the GFRP profile is bonded to the reinforced concrete T-beam by GFRP PBL connectors, which can be fixed on the GFRP profile using galvanized bolts. In this innovative composite beam, the GFRP profile can serve as main tensile resistance,

*Corresponding author, Ph.D. Candidate
E-mail: xjdxyc@foxmail.com

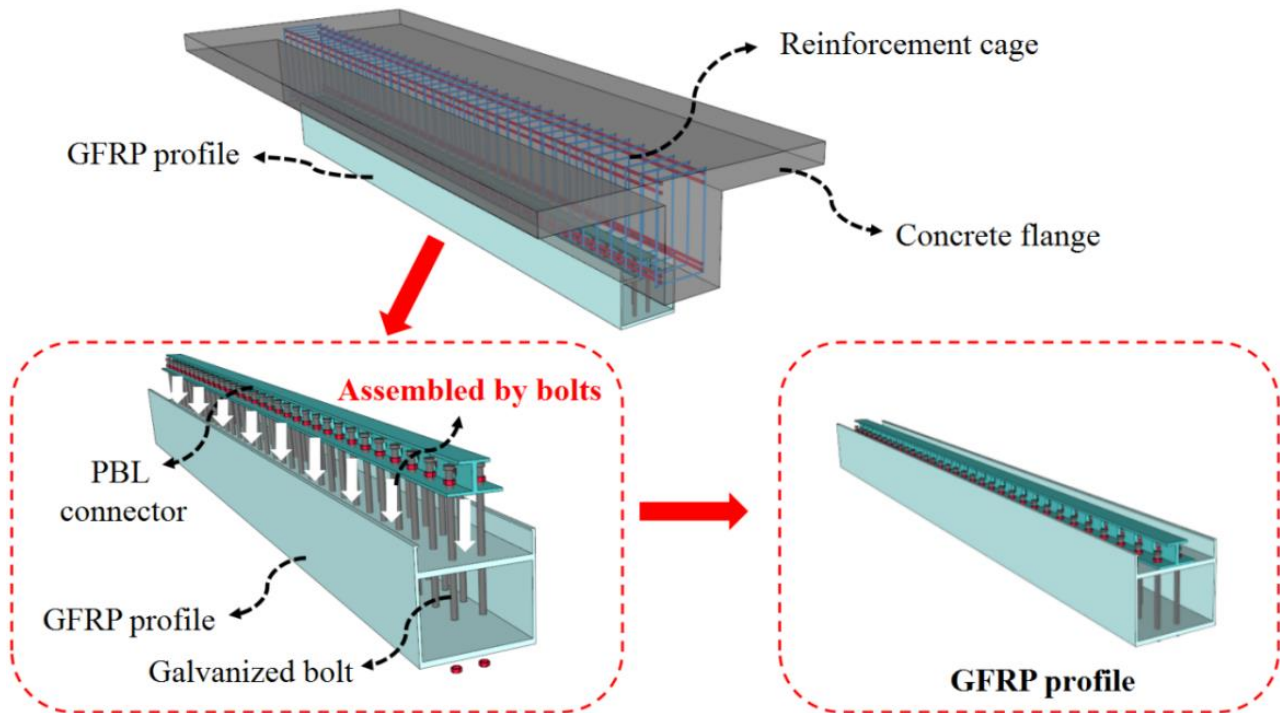


Fig. 1 Diagram of the composite beam

which can be utilized entirely in tension, by engaging the concrete part in compression, so only a small quantity of steel rebar or GFRP rebar is needed for construction. Meanwhile, the shear connectors employed here are perfobond T-shape GFRP profile, in which the concrete dowels and the top flange can efficiently avoid the slippage and vertical lift between the GFRP profile and concrete portion. Because there is a small amount of steel reinforcement in this composite beam, corrosion will be basically avoided, which makes it particularly suitable for short-span pedestrian bridges in marine areas.

This study aims to investigate the structural behaviour of this innovative composite beam. A total of eight T-beam specimens were cast and tested under three-point and four-point bending. The failure modes, flexural and shear capacity of the beam specimens were studied. Finally, based on the experimental observations and test results, corresponding calculation methods for predicting the flexural and shear capacities are put forward later in this paper.

2. Test programme

2.1 Specimen design

In this study, eight beam tests were conducted to investigate the overall structural performance of this composite beam. The main experimental variables were the beam height and the shear span-to-depth ratio. The shear span-to-depth ratio, defined as the shear span length divided by the effective height of the composite beam, which is the distance from the specimen top to the centre of the GFRP profile, was varied from 1.3 to 8.9 to investigate all the

mechanical behaviours associated with the change of shear span. The parameters of the specimens are summarized in Table 1.

The section details of the specimens are shown in Fig. 2. The length of each specimen was varied with the designed shear span, and the total beam height changes from 400 mm to 700 mm, corresponding to the dimension of full-scale pedestrian bridge girders. The specimen was composed of four parts, namely, the GFRP profile, reinforcement cage, cast-in-place concrete and GFRP PBL connectors. The PBL connectors consisted of perforated T-shape GFRP elements connected to the pultruded GFRP box profile by several galvanized bolts. The prefabricated holes (28 mm diameter) enhanced the shear stress transfer because of the concrete dowel. In order to achieve the full composite action in this composite beam, all the specimens were arranged enough shear connectors according to the former research (Yang *et al.* 2017).

Because the composite beams can be applied in the pedestrian bridges, the transversal cantilever action of the flanges in T-section of the specimens should be checked to meet the requirement of serviceability. The live load, namely the pedestrian load, can be determined as 3.5 kN/m² according to the Chinese design code (JTG D60 General Code for Design of Highway Bridges and Culverts), and the dead load, namely the dead-weight of concrete and reinforcements, can be determined as 2.5 kN/m². Through the elastic analysis, the calculated tensile stress at the cantilever bottom is 0.65 MPa, which is smaller than the tensile strength of the applied concrete, indicating that the transversal cantilever of the T-flanges could service in elastic situation.

Because the GFRP profile is weak in compressive performance, all the specimens are designed as T-beams

Table 1 Parameters of the specimens

ID	Length /mm	Height /mm	Web width /mm	Flange width /mm	Shear span /mm	Shear span-to-depth ratio λ	Concrete strength grade	Loading mode
FRCB-1	6000	400	200	1400	2900	8.9	C30	Three-point
FRCB-2	6000	500	200	1400	2900	6.8	C30	Four-point
FRCB-3	6000	600	200	1400	2900	5.5	C30	Four-point
FRCB-4	6000	700	200	1400	2900	4.6	C30	Four-point
FRCB-5	4000	400	200	1400	1900	5.8	C30	Three-point
FRCB-6	4000	500	200	1400	900	2.1	C30	Four-point
FRCB-7	1400	500	200	1400	720	1.7	C30	Three-point
FRCB-8	1100	500	200	1400	540	1.3	C30	Three-point

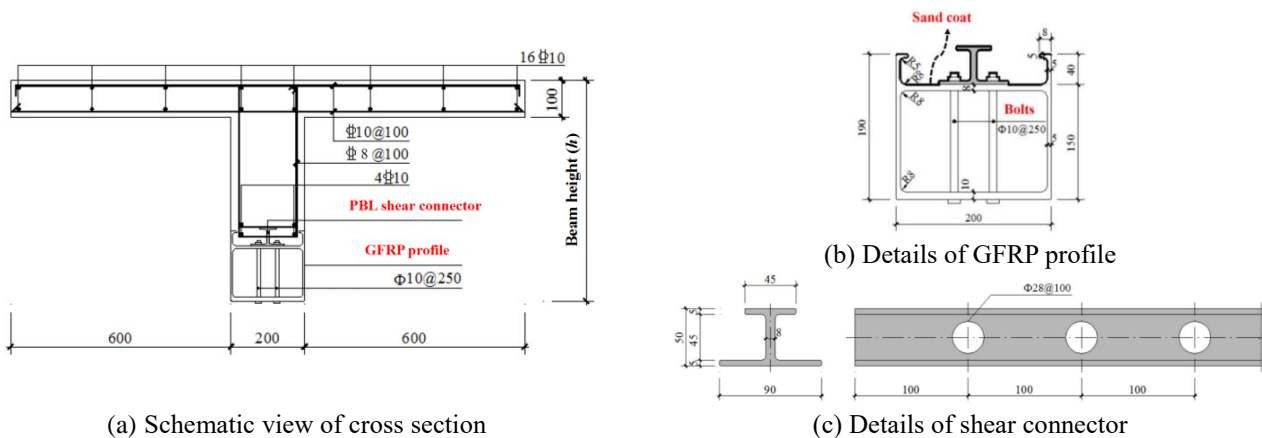


Fig. 2 Details of the composite beam

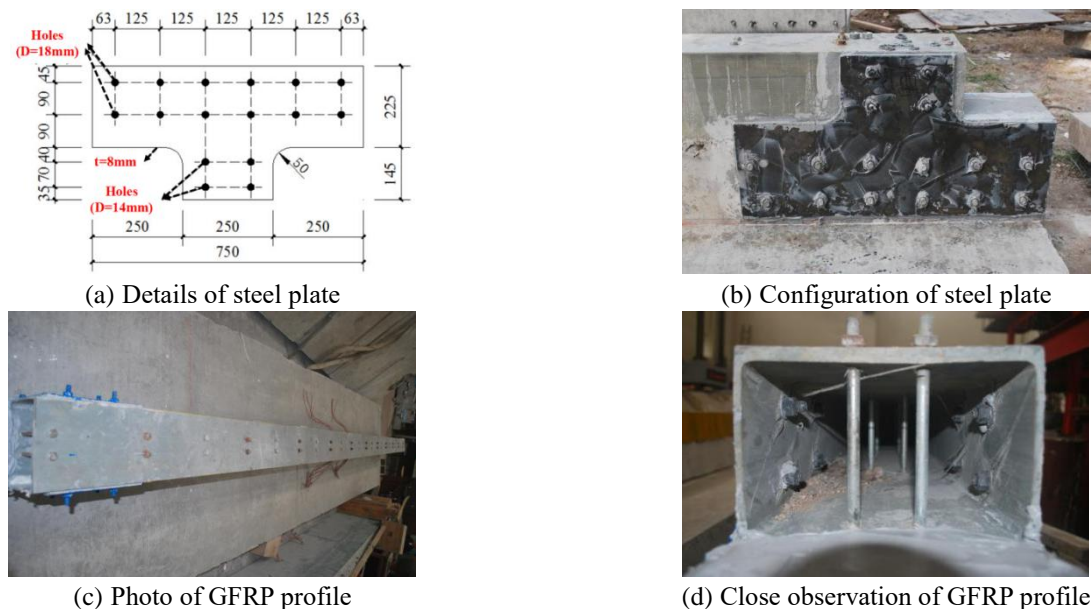


Fig. 3 Fabrication of the composite beam

with rabbets at both supports, indicating the GFRP profile is eliminated at the support area, as shown in Fig. 3(b), to solve the aforementioned problem and meanwhile to enhance the stability by decreasing the structural height of a bridge. However, local failure may occur at the rabbets because of the abrupt change in section shape, so steel plates are fixed at the sides of the support area using

structural glue and high-strength bolts to improve the local performance. Some close observations are shown in Fig. 3.

2.2 Materials

2.2.1 Concrete

The concrete strength was determined based on

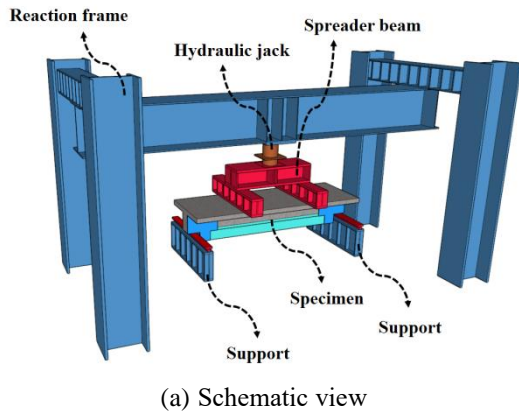
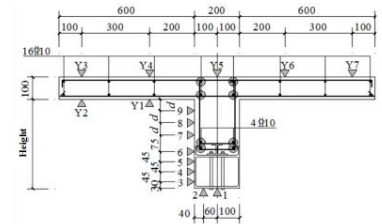
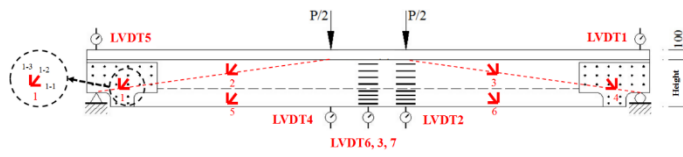
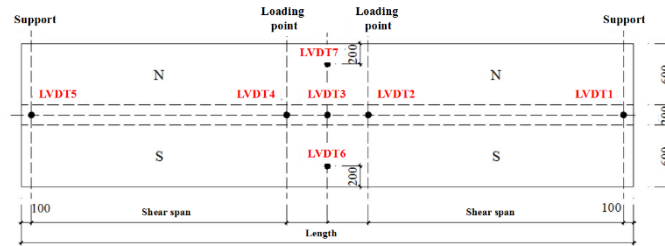


Fig. 4 Test device



(b) Lateral

(c) Cross section

Fig. 5 Layouts of LVDTs and strain gauges

compression tests of concrete samples, which were conducted according to the Chinese standard (GB 50010-2010). As presented in Table 2, test day concrete strengths of the specimens were determined through concrete cubes (150 mm×150 mm×150 mm) and prisms (150 mm×150 mm×300 mm) tests, and the average cubic compressive strength and prismatic compressive strength on the test day were 31.6 MPa and 25.6 MPa, respectively.

2.2.2 Steel reinforcement

Steel bars of HRB400 grade with diameter of 8 mm and 10 mm were used here as transverse and longitudinal reinforcement in concrete part, and the steel plates applied at the supports were 8 mm in thickness and of Q235 grade. The tensile properties of the steel reinforcements and steel plates, determined by tensile tests as per the Chinese code (GB/T228.1-2010), are listed in Table 2.

2.2.3 GFRP

The GFRP profile, matrix resin and pultrusion technique were designed as per the requirements, a woven fabric made of E-glass fibre was determined as the GFRP reinforcement, and epoxy resin was chosen as the matrix. Tensile tests were conducted according to the Chinese standard (GB/T 1447

Table 2 Material properties of steel and concrete

Material	Type	f_y /MPa	f_u /MPa	f_c /MPa	E /MPa
Concrete	C30	-	-	25.6	3.1×10^4
Steel	HRB400 (D=8 mm)	432.3	711.2	-	2.1×10^5
	HRB400 (D=10 mm)	417.1	682.5	-	2.0×10^5
	Q235 (t=8 mm)	273.6	450.3	-	2.1×10^5

Table 3 GFRP properties

GFRP material	f_u /MPa	E_{t1} /MPa	E_{t2} /MPa	G_{t12}	ν_{t12}
E-Glass fibre/epoxy resin	418.3	2.73×10^4	0.83×10^4	0.33×10^4	0.30

*The subscript 1 is the longitudinal direction of the profile; the subscript 2 is the transverse direction of the profile.

2005), and the measured GFRP strengths listed in Table 3 were determined based on the tensile tests of samples taken from the GFRP profile.

2.4 Test instrumentation

The experiment was conducted in the *Structural Engineering Key Laboratory at Xi'an University of*



(a) FRCB-1



(b) FRCB-2



(c) FRCB-3



(d) FRCB-4



(e) FRCB-5



(f) FRCB-6



(g) FRCB-7



(h) FRCB-8

Fig. 6 Tested beams at failure

Architecture and Technology. The specimens were tested under three-point bending or four-point bending until failure according to various shear span-to-depth ratios, and a 2000 kN hydraulic jack was used to apply vertically monotonic load. During the test, the vertical load was applied to the top of concrete flange by one or three

spreader beams, which meant one spreader beam was used to convert the concentrated load to distributed load in the three-point bending tests, whereas three spreader beams were needed in four-point bending tests, as shown in Fig. 4. During the test process, 7 linear variable differential transformers (LVDTs) were employed to monitor the

Table 4 Main results of FRCB-1 to FRCB-5

ID	P_u /kN	M_u /kN·m	Δ_u /mm	Failure mode	M_c /kN·m	M_c/M_u	M_{ACI} /kN·m	M_{ACI}/M_u
FRCB-1	460.83	668.20	97.74	Flexure	584.16	0.87	393.71	0.59
FRCB-2	609.47	761.84	89.37	Flexure	807.49	1.06	514.86	0.68
FRCB-3	745.35	932.43	66.87	Flexure	1035.36	1.11	636.00	0.68
FRCB-4	894.11	1117.19	58.50	Flexure	1265.94	1.13	757.14	0.68
FRCB-5	663.33	630.16	47.43	Flexure	584.16	0.93	393.71	0.62
Average ratio of measured to calculated value						1.02		0.65
Coefficient of variation						0.10		0.06

Table 5 Main results of FRCB-6 to FRCB-8

ID	P_u /kN	V_u /kN	Δ_u /mm	Failure mode	V_{cal} /kN	V_{cal}/V_u	V_{ACI} /kN	V_{ACI}/V_u
FRCB-6	770.7	385.4	21.02	Shear	367.42	0.95	316.51	0.82
FRCB-7	980.5	490.3	25.97	Shear	471.26	0.96	366.96	0.75
FRCB-8	1053.3	526.7	47.79	Shear	580.52	1.10	417.42	0.79
Average ratio of measured to calculated value						1.00		0.78
Coefficient of variation						0.07		0.04

deflections of the beam, at midpoint, two loading points, and both ends of the beam. Furthermore, a total of 25 strain gauges were glued on both sides of the concrete flange, top and bottom flanges of GFRP profile and one side of the beam at the mid-span to record the strain development, and 6 strain rosettes were mounted on the path between the support and loading point. The layouts of strain gauges and LVDTs are shown in Fig. 5.

3. Test results

3.1 Failure modes

Fig. 6 shows the failure modes of tested beams and Tables 4 and 5 list the experimental results of the tested beams. For specimens FRCB-1 to FRCB-5 with high shear span-to-depth ratios, flexural failure modes could be observed. The vertical cracks initiated approximately $0.07P_u$ to $0.2P_u$ at the mid-span, and these cracks propagated vertically with the increasing of the load. At approximately $0.3P_u$, the first diagonal crack could be captured at the shear span and developed towards the loading point. With the load increasing, new vertical cracks were observed from the mid-span to the supports. These new vertical cracks stretched inclined at approximately $0.4P_u$ to $0.5P_u$, and the cracks at mid-span vertically developed until the test ended. Slight bonding failure was observed at the end of the test with bolts distorted and longitudinal crack captured. The test finally ended owing to layer laceration of bottom of the GFRP profile.

For specimens FRCB-6 to FRCB-8 with low shear span-to-depth ratios, shear failure modes could be observed. The initial crack could be captured at the mid-span at approximately $0.1P_u$. With increasing load, some flexural cracks appeared but the crack propagations were constrained. Inclined cracks initiated at approximately

$0.4P_u$, and these cracks stretched as the load increased until the test ended. Vertical cracks at the mid-span propagated slowly and the final failure mode was dominated by the diagonal shear crack extending through the concrete flange of the critical section.

It was noticeable that no obvious local failure was found at the support area, indicating that the steel plates effectively enhanced the integrity of the support area and therefore avoided the local failure because of the rabbets. For all specimens, longitudinal cracks indicating slippage were observed on the interface only at the end of the test, which showed that the GFRP PBL connectors effectively transferred the longitudinal shear stress during the tests and all the specimens were well composite and behaved as integral members. It could be also concluded that the shear span-to-depth ratio is an essential factor which affects the failure modes of the specimens

3.2 Load-deflection curves

Fig. 7 shows the load vs. mid-span deflection responses of all the specimens. The results indicated that the shear span-to-depth ratio had the most significant influence on the behaviour of this composite beam. Generally, with the same beam height, the deformability of the specimens decreased remarkably with the decreasing of the shear span. It was also noticeable that the higher bearing capacities could be found in the specimens with lower shear span-to-depth ratios, indicating that a lower shear span-to-depth ratio correlates with higher bearing capacity at the expense of deformability. In addition, no obvious yield point could be found in all the specimens because of the linear elastic property of GFRP materials, but layer laceration, which was found in the GFRP profile at the end of the test, could be regarded as an early warning of failure.

3.3 Load-strain curves

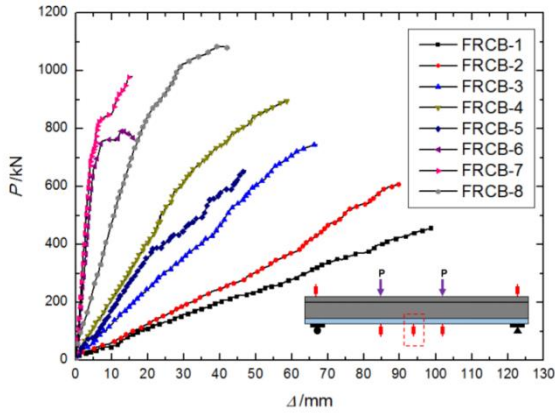


Fig. 7 Load-deflection curves

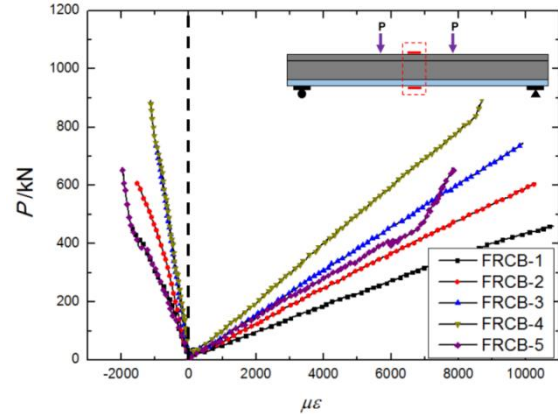


Fig. 8 Load-strain curves

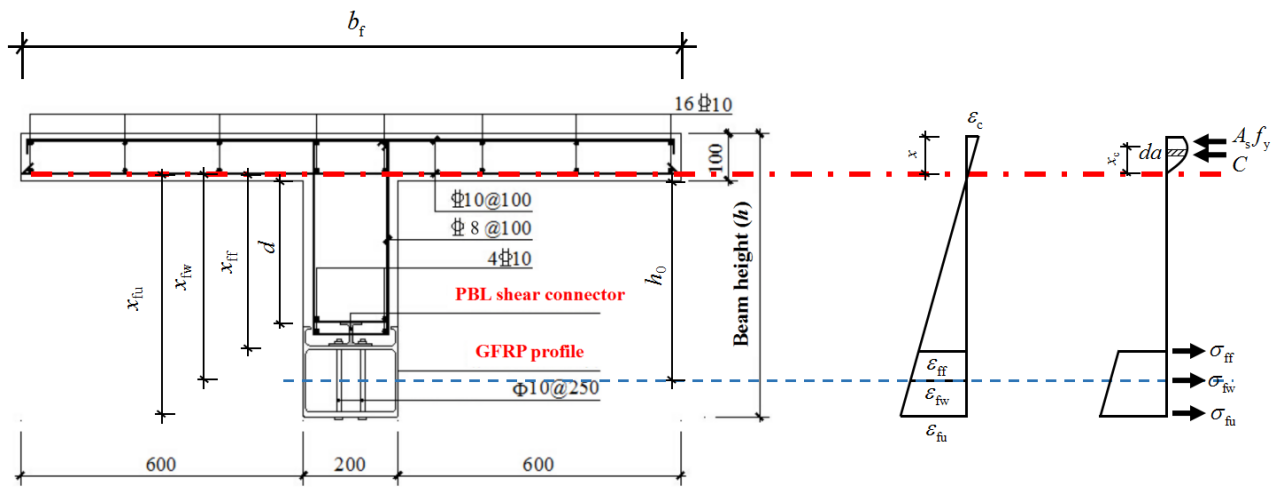


Fig. 9 Calculation diagram for flexural capacity

From the results of strain gauges attached on the concrete flange and GFRP profiles, the relationship of load and strain could be obtained, as shown in Fig. 8. For the GFRP profile, the figure clearly indicated that the strain developed linearly during the test process and the ultimate strain approached approximately 10000 $\mu\epsilon$. For concrete flange, it could be seen that the compressive strain of top concrete almost reached the peak compressive strain of concrete, approximately -2000 $\mu\epsilon$.

3.4 Load-shear stress curves of steel plates

To evaluate the contribution of steel plate to the overall shear capacity of the specimens, the relationship between the applied vertical load and strain of steel plates was monitored, and the shear stress of the steel plates could be determined by the strain results of strain rosettes

$$\tau = \frac{E}{(1+\nu)} \sqrt{\left(\frac{\epsilon_0 - \epsilon_{90}}{2}\right)^2 + \left(\frac{2\epsilon_{45} - \epsilon_0 - \epsilon_{90}}{2}\right)^2} \quad (1)$$

where ϵ_0 is the strain determined by the longitudinal gauge of the rosette, ϵ_{45} is the strain determined by the diagonal gauge of the rosette, and ϵ_{90} is the strain determined by the vertical gauge of the rosette.

This indicated that all steel plates did not reach the yield stress, and the shear stresses of the steel plates at the end of the tests of FRCB-6, FRCB-7 and FRCB-8 were 26.7 MPa, 43.3 MPa and 59.9 MPa, respectively.

3.5 Longitudinal shear transfer

Due to the absence of the slippage measurement instruments, the precise longitudinal shear stress could not be obtained by this test, but the theoretical longitudinal shear stress on the interface can be obtained by elastic analysis, in which the section-conversion method should be used. In the elastic analysis, the longitudinal shear stress on the interface per unit length can be determined by the following equation

$$V_{\text{longitudinal}} = \frac{V_{\text{vertical}} S_0}{I_0} \quad (2)$$

where $V_{\text{longitudinal}}$ is the longitudinal shear stress on the interface; V_{vertical} is the applied vertical load at the loading point; S_0 is the area moment of the concrete section; I_0 is the inertia moment of the entire converted section.

It can be found from the analysis that the longitudinal shear stress on the interface increases with the increasing of

the applied vertical load. In another word, the variation of the neutral axis depth in the section can be caused by the variation of the applied vertical load, and the variation of the applied vertical load will lead to the variation of the longitudinal shear stress on the interface. The maximum shear stress transfer can be captured when the specimens are loaded to the corresponding maximum vertical loads. There was no obvious slippage on the interface between the concrete part and the GFRP profile in all the specimens when loaded to the maximum loads, indicating that all the specimens were well composite.

4. Analysis of flexural capacity

4.1 Basic assumptions

During the test, bonding cracks between the GFRP profile and concrete part were only observed at the end of the test, which indicated that the specimens could be regarded as properly composite. Because GFRP material is generally assumed to be a kind of linearly elastic material, the theory of elasticity is applied here to analyse the flexural capacity. Some simple assumptions can be summarized as follows:

- (1) The plane-section hypothesis was satisfied.
- (2) The tensile strength of the concrete was neglected.
- (3) Because the top concrete in the specimens only reached the peak compressive strain in the tests, the Hognestad constitutive law was adopted to describe the compressive behaviour of concrete for simplification.
- (4) The ultimate strain of the GFRP plate was limited to $10000 \mu\epsilon$ according to the test results, namely, $\epsilon_{fu}=10000 \mu\epsilon$. The calculation diagram is presented in Fig. 9.

4.2 Calculation procedure

The flexural capacity varies with the strain of the top concrete. To simplify the design procedure, two different cases were defined here to calculate the flexural capacity, of which one case had the neutral axis passing through the concrete flange and the compressive strain of top concrete being smaller than the peak compressive strain of concrete, while the other case had the neutral axis passing through the web of the T-beam. The test results indicated that all the specimens failed according to the first case, so the first case was discussed here.

The stress of the concrete and the GFRP profile (flanges and webs of GFRP box profile) can be obtained as follows

$$\sigma_c = f_c \frac{\epsilon_c}{\epsilon_0} \left(2 - \frac{\epsilon_c}{\epsilon_0}\right) \quad (3)$$

$$\sigma_{fu} = E_f \epsilon_{fu} \quad (4)$$

$$\sigma_{fw} = E_f \epsilon_{fw} \quad (5)$$

$$\sigma_{ff} = E_f \epsilon_{ff} \quad (6)$$

The resultant of the concrete flange can be calculated as

$$C = \int_0^x f_c \left[\frac{\epsilon_c}{\epsilon_0} \left(2 - \frac{\epsilon_c}{\epsilon_0}\right) \right] b_f da = \frac{5x^2(3h-8x)}{3(h-x)^2} f_c b_f \quad (7)$$

Therefore, the depth of the concrete compressive zone can be obtained as

$$C = f_y A_s (x - a_s) + E_f \epsilon_{fu} + E_f \epsilon_{fw} + E_f \epsilon_{ff} \quad (8)$$

The distance from the neutral axis to the resultant point of the concrete can be determined as

$$x_c = \frac{1}{C} \int_0^x f_c \left[\frac{\epsilon_c}{\epsilon_0} \left(2 - \frac{\epsilon_c}{\epsilon_0}\right) \right] b_f a da = x \left[\frac{8h-23x}{4(3h-8x)} \right] \quad (9)$$

Finally, the flexural capacity of the specimens can be calculated as

$$M_c = C x_c + f_y A_s (x - a_s) + E_f \epsilon_{fu} x_{fu} + E_f \epsilon_{fw} x_{fw} + E_f \epsilon_{ff} x_{ff} \quad (10)$$

The method of ACI 440 is also applied here because of its simplicity in determining the flexural capacity, and the flexural capacity of the specimens can be calculated by Eqs. (11)-(12). In these equations, f_u is defined the same as σ_{fu} in Eq. (4) according to the test result that the tensile strain of the GFRP profile in the static test is less than tensile strain of tensile samples owing to the layer laceration.

$$M_{ACI} = A_r f_u \left(h_0 - \frac{\beta_1 c}{2} \right) h_0 \quad (11)$$

$$c = \left(\frac{\epsilon_{cu}}{\epsilon_{cu} + \epsilon_{fu}} \right) \quad (12)$$

The measured and calculated results for the proposed method and ACI 440 method were tabulated in Table 4. It can be seen that the proposed method could reasonably predict the flexural capacity, although it slightly overestimates the flexural capacity in some specimens. Meanwhile, the ACI 440 method is excessively conservative compared with the proposed method.

5. Analysis of shear capacity

The shear capacity of the specimens can be obtained using the following equation

$$V_{cal} = \mu(V_c + V_s) + V_{sp} \quad (13)$$

where V is the overall shear capacity, V_c is the shear capacity of the concrete portion, V_s is the shear capacity of the stirrups, V_{sp} is the contribution of the steel plates, and μ is the coefficient to take the contribution of T-shape concrete flange to the reinforced concrete part into account, with Placas *et al.* (1971) proposing that $\mu=1.25$.

For the concrete portion, Choi *et al.* (2007) proposed a unified shear strength model for reinforced concrete beams

and it has been verified to be valid by the verification of a compiled database of RC beams. The GFRP profile here is employed to be longitudinal reinforcement, and the shear mechanism of this composite beam was similar to that of RC beams. Therefore, the model proposed by Choi *et al.* was applied and modified here to calculate the shear capacity of the specimens. The shear capacity of the concrete part can be determined by Eqs. (14)-(15)

$$V_c = 0.52\sqrt{f_c} b [c_{(\alpha_{x1}\varepsilon_0)} - c_c] + 0.45f_c b c_c \quad (14)$$

$$c_c = (1 - 0.43\lambda)c_{(\alpha_{x1}\varepsilon_0)} \quad (15)$$

Here, $c_{(\alpha_{x1}\varepsilon_0)}$ is the depth of the compression zone at the critical section, and the subscript $\alpha_{x1}\varepsilon_0$ denotes the compressive strain of top concrete at the critical section. c_c is the depth of the compression zone at the loading section. The value of $c_{(\alpha_{x1}\varepsilon_0)}$ can be obtained by equilibrium of resultant of tensile GFRP profile and resultant of compressive concrete as follows

$$A_f \alpha_{x1} \varepsilon_0 \frac{(h_0 - c_{(\alpha_{x1}\varepsilon_0)})}{c_{(\alpha_{x1}\varepsilon_0)}} h_0 E_f = b \int_0^{c_{(\alpha_{x1}\varepsilon_0)}} f_c [2 \frac{\varepsilon}{\varepsilon_0} - (\frac{\varepsilon}{\varepsilon_0})^2] d\varepsilon \quad (16)$$

$c_{(\alpha_{x1}\varepsilon_0)}$ can be obtained by solving Eq. (16)

$$c_{(\alpha_{x1}\varepsilon_0)} = h_0 \frac{\sqrt{(E_f \alpha_{x1} \varepsilon_0 \rho_f)^2 + 4E_f \alpha_{x1} \varepsilon_0 \rho_f (\alpha_{x1} - \frac{\alpha_{x1}^2}{3}) f_c - E_f \alpha_{x1} \varepsilon_0 \rho_f}}{2(\alpha_{x1} - \frac{\alpha_{x1}^2}{3}) f_c} \quad (17)$$

Therefore, the shear capacity of the concrete part can be determined through Eqs. (14)-(17).

For the steel plates, the measured shear stress in the tests were applied here, and the shear capacity of steel plates can be obtained as

$$V_{sp} = 2\tau t h_s \quad (18)$$

For the stirrups, the shear capacity of shear reinforcement V_s is defined as

$$V_s = \frac{A_{sv}}{s} f_{yv} d \quad (19)$$

Finally, the shear capacity of this composite beam can be determined by solving the resulting Eqs. (13)-(19) simultaneously. Table 5 tabulates the measured and calculated results for the proposed method, and the average value of the ratios of the test results to the capacities predicted by the proposed method is 1.00, with a coefficient of variation of 0.07. This result indicates that the proposed method can accurately predict the shear capacity of this composite beam, although it slightly overestimates the shear capacity of the specimen FRCB-8, which has a relatively low shear span-to-depth ratio. Furthermore, the ACI 440 method is also used here to predict the shear capacity of the concrete part of the specimens using Eqs. (20)-(21), and the

corresponding results are listed in Table 5. It can be seen that the method of ACI 440 underestimates the shear capacity of the concrete part compared with the proposed method.

$$V_{ACI} = \mu \left(\frac{2}{5} \sqrt{f_c} b k h_0 + \frac{A_{sv}}{s} f_{yv} d \right) + V_{sp} \quad (20)$$

$$k = \sqrt{2\rho_f n_f + (\rho_f n_f)^2} - \rho_f n_f \quad (21)$$

6. Conclusions

This paper presents the results of static tests on eight GFRP-concrete composite beams. The main parameters examined in this study are the shear span-to-depth ratio and the height of the composite beam. Theoretical models were used to predict the flexural and shear capacity of the tested beams. Based on the results, the following conclusions can be drawn:

- The failure patterns of the specimens varied with the shear span-to-depth ratio. Five specimens with high shear span-to-depth ratios failed in flexure, and the other three specimens with low shear span-to-depth ratios failed in shear.

- Because of the linear elasticity of the GFRP material, all the specimens suffered slightly brittle behaviour in the failure stage with a high load-bearing capacity. However, the development of split-tear cracks and layer laceration, which was found in the GFRP profile at the end of the test, could be regarded as an early warning of final failure.

- The GFRP PBL connectors played an important role in transferring the stress at the interface of the GFRP and concrete portion, and bonding cracks did not occur at the interface between the GFRP profile and the concrete until the last stage of the test, which indicated that the specimens performed well as composite beams. Due to the absence of the slippage measurement instruments, the precise longitudinal shear stress on the interface between the two different materials could not be obtained by this test. Although the longitudinal shear transfer was analyzed through elastic method in this paper, further push-out tests and structural tests on the mechanical behaviors of the GFRP PBL connectors should be conducted to form a thorough design method for this shear connector.

- Based on the experimental results, methods for determining the flexural capacity and shear capacity of this composite beam are proposed. A comparative study shows that the proposed methods can reasonably predict both the flexural and shear capacity of these composite beams. On the other hand, the ACI 440 methods were relatively conservative.

Acknowledgements

The experiments conducted in this study were sponsored by the National Key Research and Development Program of China (Grant No. 2017YFC0703404) and the National

Natural Science Foundation of China (Grant No. 50978107). Their support is greatly appreciated.

References

- ACI 440R (2006), *Guide for the Design and Construction of Structural Concrete Reinforced with FRP Bars*, American Concrete Institute, Michigan, U.S.A.
- Aydin, F. and Sarıbyık, M. (2013), "Investigation of flexural behaviors of hybrid beams formed with GFRP box section and concrete", *Constr. Build. Mater.*, **41**(2), 563-569.
- Choi, K.K., Park, H.G. and Wight, J.K. (2007), "Unified shear strength model for reinforced concrete beams-part i: Development", *ACI Struct. J.*, **104**(2), 142-152.
- Choi, K.K. and Park, H.G. (2007), "Unified shear strength model for reinforced concrete beams-part ii: Verification and simplified method", *ACI Struct. J.*, **104**(2), 153-161.
- Fam, A. and Skutezky, T. (2006), "Composite T-beams using reduced-scale rectangular FRP tubes and concrete slabs", *J. Compos. Constr.*, **10**(2), 172-181.
- GB 50010 (2010), *Code for Design of Concrete Structures*, MoHURD, Beijing, China.
- GB/T228.1 (2010), *Metallic Materials-Tensile Testing-Part 1: Method of Test at Room Temperature*, AQSIQ, Beijing, China.
- GB/T 1447 (2005), *Fiber-Reinforced Plastics Composites-Determination of Tensile Properties*, AQSIQ, Beijing, China.
- Hadi, M.N.S. and Yuan, J.S. (2017), "Experimental investigation of composite beams reinforced with GFRP I-beam and steel bars", *Constr. Build. Mater.*, **144**, 462-474.
- Hassanzadeh, A.M. and Dehestani, M. (2017), "Numerical modeling of semi-confined composite beams consisting of GFRP and concrete", *Struct. Eng. Mech.*, **62**(1), 79-84.
- Huang, L., Zhang, C., Yan, L. and Kasal, B. (2017), "Flexural behavior of U-shape FRP profile-RC composite beams with inner GFRP tube confinement at concrete compression zone", *Compos. Struct.*, **184**, 674-687.
- JTG D60 (2015), *General Code for Design of Highway Bridges and Culverts*, MoT, Beijing, China.
- Koalk, A., Bel, S. and Jurkiewicz, B. (2017), "Experimental tests and analytical model of concrete-GFRP hybrid beams under flexure", *Compos. Struct.*, **180**, 192-210.
- Muttashar, M., Manalo, A., Karunasena, W. and Lokuge, W. (2017), "Flexural behaviour of multi-celled GFRP composite beams with concrete infill: Experiment and theoretical analysis", *Compos. Struct.*, **159**, 21-33.
- Neagoe, C.A., Gil, L. and Pérez, M.A. (2015), "Experimental study of GFRP-concrete hybrid beams with low degree of shear connection", *Constr. Build. Mater.*, **101**, 141-151.
- Placas, A., Regan, P.E. and Baker, A.L. (1971), "Shear failure of reinforced concrete beams", *ACI*, **68**(10), 763-773.
- Thomas, J. and Ramadassa, S. (2015), "Design for shear strength of concrete beams longitudinally reinforced with GFRP bars", *Struct. Eng. Mech.*, **53**(1), 41-55.
- Unsal, I., Tokgoz, S., Cagatay, I.H. and Dundar, C. (2017), "A study on load-deflection behavior of two-span continuous concrete beams reinforced with GFRP and steel bars", *Struct. Eng. Mech.*, **63**(5), 629-637.
- Wight, J.K. (2011), *Reinforced Concrete: Mechanics and Design*, Pearson Publishing Ltd, New Jersey, U.S.A.
- Xin, H., Liu, Y., He, J., Fan, H. and Zhang, Y. (2015), "Fatigue behavior of hybrid GFRP-concrete bridge decks under sagging moment", *Steel Compos. Struct.*, **18**(4), 925-946.
- Yang, Y., Xue, Y., Yu, Y., Liu, R. and Ke, S. (2017), "Study of the design and mechanical performance of a GFRP-concrete composite deck", *Steel Compos. Struct.*, **24**(6), 679-688.

- Zuo, Y., Liu, Y. and He, J. (2018), "Experimental investigation on hybrid GFRP-concrete decks with T-shaped perforated ribs subjected to negative moment", *Constr. Build. Mater.*, **158**, 728-741.

CC

Notation

A_f	Cross-sectional area of GFRP profile;
A_{sv}	Cross-sectional area of stirrup;
A_s	Area of longitudinal steel rebar in concrete flange;
a_s	Thickness of concrete cover;
b_f	Width of concrete flange;
b	Width of concrete web;
d	Effective height of concrete part;
E_f	Modulus of elasticity of GFRP profile;
E_c	Modulus of elasticity of concrete;
f_c	Compressive strength of concrete;
f_y	Yield strength of longitudinal steel rebar;
f_{yv}	Yield strength of stirrup;
f_{fu}	Effective tensile strength of GFRP profile;
h	Total height of composite beam;
h_0	Effective height of composite beam;
h_s	Effective height of steel plate, which can be obtained by total height of steel plate, deducting the diameter of bolt holes;
I_0	Inertia moment of the entire converted section;
M_u	Peak moment of specimen;
M_{ACI}	Calculated flexural capacity by ACI 440 method;
M_c	Calculated flexural capacity by proposed method;
n_f	E_f / E_c ;

P_u	Peak load of specimen;
s	Spacing of stirrup;
S_0	Area moment of the entire concrete section;
t	Thickness of steel plate;
V_u	Peak shear capacity of specimen;
V_{cal}	Calculated shear capacity by proposed method;
V_{ACI}	Calculated shear capacity by ACI 440 method;
$V_{longitudinal}$	Longitudinal shear stress on the interface;
$V_{vertical}$	Applied vertical load at the loading point;
ε_0	Peak compressive strain of concrete, $\varepsilon_0=0.002$;
ε_{fu}	Tensile strain of bottom flange of GFRP profile;
ε_{ff}	Tensile strain of top flange of GFRP profile;
ε_{fw}	Tensile strain of web of GFRP profile;
ε_{cu}	Ultimate compressive strain of concrete;
ρ_f	Ratio of GFRP profile, $\rho_f=A_f/bh$;
Δ_u	Ultimate deflection at mid-span;
β_1	Factor taken as 0.85 for concrete strength;
τ	Measured shear stress of steel plate.